The Astrophysical Journal Letters, 727:L43 (6pp), 2011 February 1 doi:10.1088/2041-8205/727/2/L43

CASE STUDY OF FOUR HOMOLOGOUS LARGE-SCALE CORONAL WAVES OBSERVED ON 2010 APRIL 28 AND 29

I. W. Kienreich[1], A. M. Veronig[1], N. Muhr[1], M. Temmer[1,2], B. Vršnak[3], and N. Nitta[4]
[1] Institute of Physics, University of Graz, Universitätsplatz 5, A-8010 Graz, Austria; ines.kienreich@uni-graz.at
[2] Space Research Institute, Austrian Academy of Sciences, Schmiedlstraße 6, A-8042 Graz, Austria
[3] Hvar Observatory, Faculty of Geodesy, Kačićeva 26, 1000 Zagreb, Croatia
[4] LMSAL, 3251 Hanover Street, Palo Alto, CA 94304, USA
Received 2010 October 6; accepted 2010 December 15; published 2011 January 12

ABSTRACT

On 2010 April 28 and 29, the *Solar TErrestrial Relations Observatory B*/Extreme Ultraviolet Imager observed four homologous large-scale coronal waves, the so-called EIT-waves, within 8 hr. All waves emerged from the same source active region, were accompanied by weak flares and faint coronal mass ejections, and propagated into the same direction at constant velocities in the range of ∼220–340 km s^{-1}. The last of these four coronal wave events was the strongest and fastest, with a velocity of 337 ± 31 km s^{-1} and a peak perturbation amplitude of ∼1.24, corresponding to a magnetosonic Mach number of $M_{\rm ms} \sim 1.09$. The magnetosonic Mach numbers and velocities of the four waves are distinctly correlated, suggestive of the nonlinear fast-mode magnetosonic wave nature of the events. We also found a correlation between the magnetic energy buildup times and the velocity and magnetosonic Mach number.

Key words: Sun: corona – Sun: coronal mass ejections (CMEs) – Sun: flares

Online-only material: animations

1. INTRODUCTION

Large-scale propagating disturbances in the solar corona have been the subject of extensive studies for more than 12 years. These events were observed for the first time by the Extreme-ultraviolet Imaging Telescope (EIT; Delaboudinière et al. 1995) on board the *Solar and Heliospheric Observatory* (*SOHO*; Moses et al. 1997; Thompson et al. 1998) and are thus commonly called "EIT-waves." They appear as diffuse coronal brightenings, forming circular wave fronts, traveling hundreds of megameters without hindrance under quiet-Sun conditions.

At present there are two competing groups of models based on completely different ideas of the physical nature of EIT, or more generally, EUV waves. The first theory describes them as nonlinear fast-mode magnetosonic waves following the original interpretation of large-scale disturbances by Uchida (e.g., Thompson et al. 1998; Wills-Davey & Thompson 1999; Wang 2000; Klassen et al. 2000; Wu et al. 2001; Vršnak et al. 2002; Warmuth et al. 2004; Veronig et al. 2006). Several characteristics of coronal waves can be explained by this theory: (1) the propagation perpendicular to magnetic field lines (e.g., Thompson et al. 1998), (2) the pulse broadening and amplitude drop off (Wills-Davey 2006; Warmuth 2010; Veronig et al. 2010), and (3) the reflection and refraction at regions of high Alfvén velocity (Thompson et al. 1999; Veronig et al. 2008; Long et al. 2008; Gopalswamy et al. 2009). The second group of models, however, considers these coronal bright fronts as no waves at all, but as the signature of a large-scale magnetic reconfiguration of field lines during a coronal mass ejection (CME) lift-off (e.g., Delannée & Aulanier 1999; Chen et al. 2002; Attrill et al. 2007). In these pseudo-waves models, coronal waves could exclusively occur in conjunction with CMEs. This assumption is supported by statistical studies, showing a close relation between waves and CMEs (e.g., Biesecker et al. 2002). These models can also explain stationary brightenings (Delannée & Aulanier 1999; Cohen et al. 2009) and the occasionally observed rotation of coronal bright fronts (Podladchikova & Berghmans 2005). For recent reviews we refer to Vršnak & Cliver (2008), Wills-Davey & Attrill (2009), and Warmuth (2010).

The limitations of EIT observations, especially the low imaging cadence of ∼12–15 minutes, were a major contributor to the difficulties determining the physical nature of coronal waves. The Extreme Ultraviolet Imager (EUVI; Wuelser et al. 2004) instruments, which are part of the Sun Earth Connection Coronal and Heliospheric Investigation (SECCHI; Howard et al. 2008) suite on board the twin *Solar-TErrestrial Relations Observatory* (*STEREO*; Kaiser et al. 2008) spacecraft, overcome these limitations. EUVI observes the entire solar disk as well as the corona up to 1.7 $R_\odot$ in four spectral channels (He II 304 Å: $T \sim 0.07$ MK; Fe IX 171 Å: $T \sim 1$ MK; Fe XII 195 Å: $T \sim 1.5$ MK; Fe XV 284 Å: $T \sim 2.25$ MK). The high imaging cadence down to ∼75 s, and the large field of view (FoV) as well as the ability of simultaneous observations from two vantage points provide us with new insights into the three-dimensional kinematics and dynamics of EUV waves (e.g., Kienreich et al. 2009; Patsourakos & Vourlidas 2009; Veronig et al. 2010). In this Letter, we present the first case of homologous EIT waves ever reported in the nearly 14 years of continuous studies of large-scale coronal waves. The four homologous waves, observed by *STEREO-B* within a period of 8 hr, were launched from the same active region (AR), propagated in the same direction, and their wave fronts were similar in both shape and angular extent. These events allow us to perform a detailed study of the physical characteristics of large-scale coronal waves, as these homologous waves are initiated and propagate under similar coronal background conditions. Hence, our analysis of the correlation between the wave pulse parameters is not influenced by the limiting factor of differing coronal plasma conditions, persistent in previous comparative studies of EIT waves.

2. DATA

The events under study occurred on 2010 April 28 and 29, and were observed by *STEREO-B* (henceforth *ST-B*),

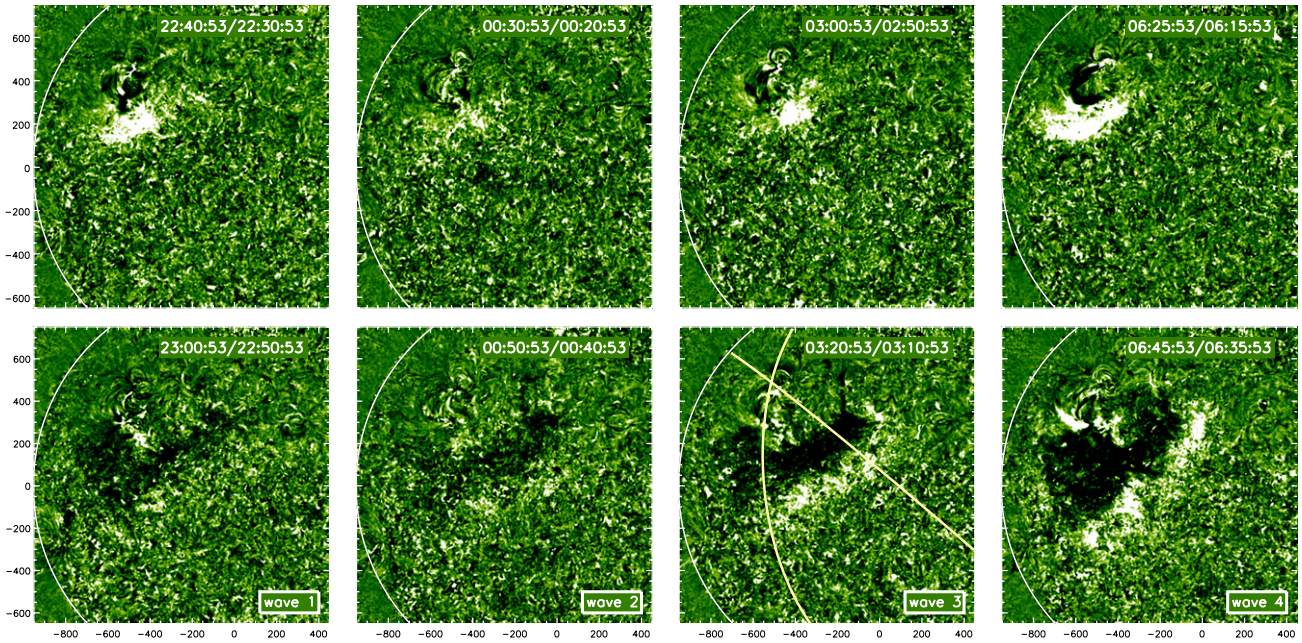

Figure 1. Median-filtered 10 minute running ratio images recorded in EUVI-B 195 Å showing the early evolution of four homologous waves on 2010 April 28 and 29 (axes in arcsec). Each column consists of two images recorded 20 minutes apart of one particular event. Upper panel: wave fronts at the time of the peak perturbation amplitudes (see accompanying animation 1). Panel 7: yellow meridians define the sector, for which the wave kinematics was analyzed.

(An animation of this figure is available in the online journal.)

positioned 70°5 behind Earth on its orbit around the Sun. For our analysis, only the high-cadence EUVI imagery in 195 Å (cadence of 5 minutes) was suitable, since the 171 Å and 284 Å filtergrams were recorded only every 2 hr, and the 304 Å data revealed no wave signatures at all. In addition, the white-light coronagraph images of the COR1-B and COR2-B instruments (Howard et al. 2008) and of the Large Angle and Spectrometric COronagraph (LASCO; Brueckner et al. 1995) C2 instrument on board *SOHO* were used to identify signatures of associated CMEs. The EUVI 195 Å filtergrams were reduced using the SECCHI_PREP routines available within Solarsoft. Additionally, we differentially rotated the images to the same reference time. In order to enhance faint coronal wave signatures, we derived running ratio (RR) images dividing each direct image by a frame taken 10 minutes earlier.

3. RESULTS

3.1. Wave Characteristics

The four EUV waves under study were launched on 2010 April 28 and 29 within a period of 8 hr (see Figure 1). Animation 1 shows *ST-B* 195 Å direct and RR full disk images covering the full observation period. Figure 1 consists of snapshots from the animation illustrating the evolution of all four waves. In each column, we present two fronts of each event, with the upper panels showing the wave front with the maximum intensity amplitude and the lower panels showing the propagating wave front 20 minutes later. All four coronal disturbances are launched from the same AR NOAA 11067, propagate in the same direction, and have a similar appearance and angular extent, thus it is appropriate to call them homologous. The time interval between the onsets of the successive waves steadily increased: ∼1.75 hr (waves 1 and 2), ∼2.5 hr (waves 2 and 3), and ∼3.5 hr (waves 3 and 4). In order to obtain better insight into the onset of the coronal waves, we studied a small area (FoV: 600″ × 600″) centered on the source AR. Figures 2((f) and (g)) give one snapshot of this region during the launch of wave 4, the strongest one of the four events. During the full observation period, we recorded persisting dynamical processes in the extended loop system of NOAA 11067 (see animation 2A available in the online version of the journal).

The resemblance of the events suggests that the background coronal field has not changed noticeably within these 8 hr. Moreover, this implies that the corona is disturbed by the EIT waves only for a short period of time and returns to its pre-event condition on a timescale of tens of minutes. In at least two cases, waves 3 and 4, there is evidence that the main perturbation was followed by an additional weak disturbance about 20 minutes later (see animation 1).

3.2. Wave Kinematics and Perturbation Characteristics

We analyzed the kinematics of the waves, each treated as unique event, employing two different methods. First, we visually determined the wave fronts in a series of RR images. Second, we examined the perturbation amplitudes of the wave. In both methods, we focused on a 60° sector on the solar surface, where all four waves were distinctly observable (see Figure 1, panel 7; yellow curves).

In the first method, the wave fronts were tracked manually, and their center was obtained from a circular fit to the earliest wave fronts carried out in spherical coordinates (see Veronig et al. 2006). The mean distance of each wave front from the thus determined center is calculated along the solar surface. In the second method, we subdivided the solar surface into spherical segments of equal width concentric around the wave center obtained by method one. Plotting the average intensities versus mean distances of all segments gives one intensity profile per RR image (cf. Muhr et al. 2010). In these perturbation profiles, shown in Figure 4 (top panels), the wave front presents itself as distinct bump above the background intensity. In each case, the perturbation amplitude reaches its maximum ∼5 minutes after the onset of the wave (see Figure 4). As example, the

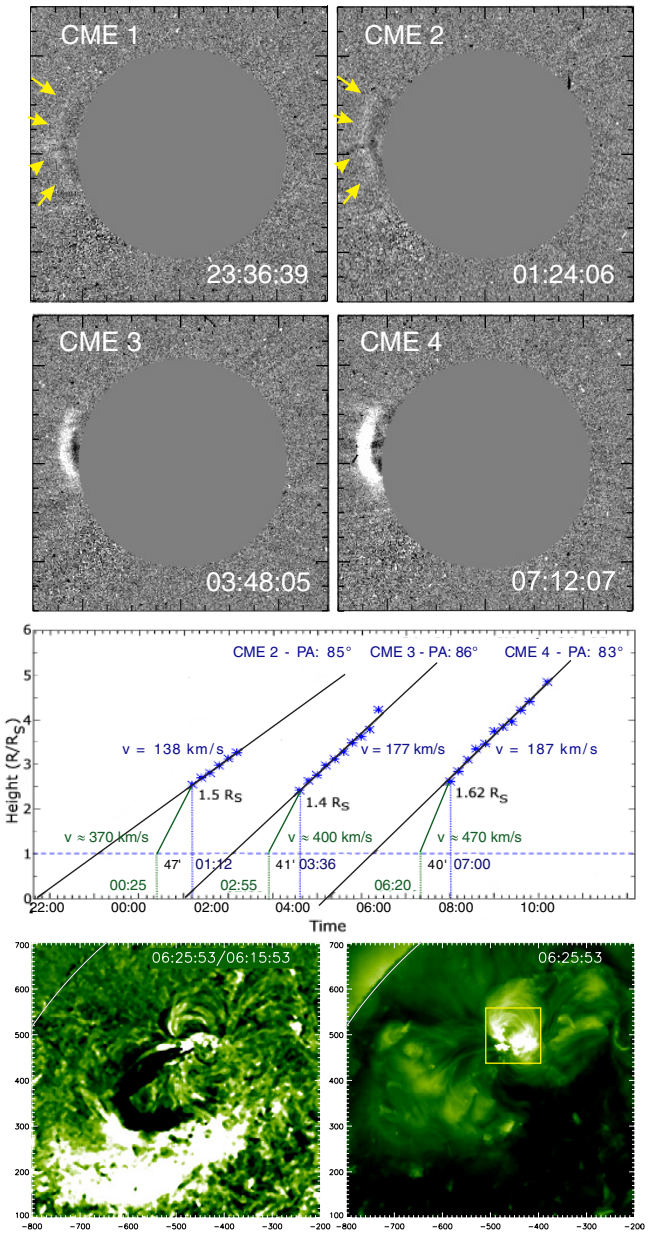

Figure 2. Associated features: (a)–(d) LASCO C2 running difference images of associated weak CMEs at the time of the maximum leading edge intensity (cf. animation 2B). (e) Kinematics of CMEs 2–4 in C2 (blue stars), plus estimated initial CME speed (green lines) by setting the moment of the first observed associated wave front as CME onset time. CME 1 was too faint to be measured. (f) Median-filtered EUVI-B 195 Å running ratio image at 06:25 UT showing the early phase of wave 4 and the disappearance of an AR loop system (axes in arcsec). (g) Co-temporal direct image revealing an intensity increase of the inner loop system of AR 11067 and the associated flare (cf. animation 2A). Yellow square: $110'' \times 110''$ subfield used to analyze flare intensity variations.

(Animations [A, B] of this figure are available in the online journal.)

evolution of the perturbation amplitude of wave 4 is plotted in Figure 3 (bottom panel). From the wave perturbation profiles, we extracted the foremost position of the wave front, defined as the point at which the Gaussian fit to the profile falls below the value of $I/I_0 = 1.02$ (blue dotted line in top panel of Figure 4). We note that the visually tracked distances match well the position of the wave front obtained from the perturbation profiles (Figure 4).

In Figure 3 (top panel), we show the kinematics for wave 4 derived with both methods together with error bars. Linear as well

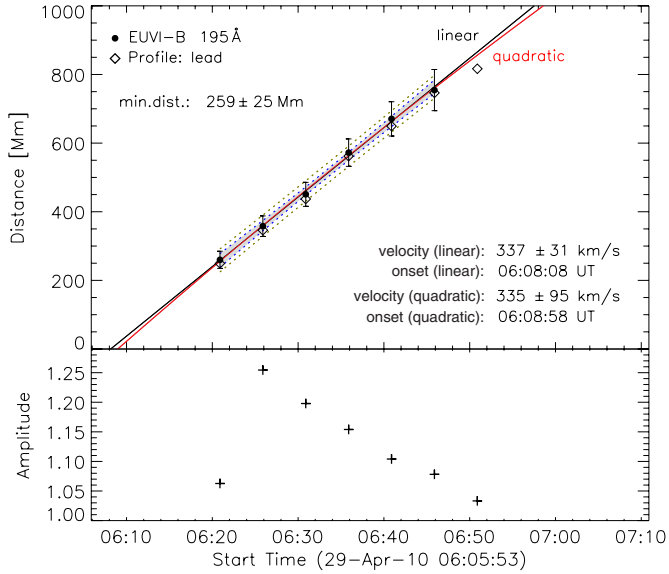

Figure 3. Top: kinematics of wave 4 determined by two methods plus error bars reflecting the diffusiveness of the wave fronts. Kinematics of the visually determined wave fronts in 195 Å represented by black circles of the Gaussian-fitted perturbation profile by diamonds. A linear (black) and a quadratic (red) least-square fit are overlaid. The gray area indicates the 95% confidence interval of the linear fit. Bottom: evolution of the perturbation amplitude determined from EUVI-B 195 Å intensity profiles in units of pre-event intensity I_0 (compare Figure 4, top panels).

as quadratic least-squares fits were applied to the time–distance data, both yielding similar velocities of $\sim$340 km s^{-1}. The parabolic fit suggests a small deceleration of -10 m s^{-2}. In order to distinguish whether the linear or parabolic fit better represents the data, we derived the 95% confidence interval for the linear fit. The quadratic fit lies within the error bars and the confidence interval, thus it is reasonable to represent the wave's kinematics by the linear fit with a constant velocity of 337 ± 31 km s^{-1} over the full propagation distance up to 800 Mm.

We found similar results for the other three wave events under study, which is illustrated in Figure 4 (bottom panels). The velocities v_c of the four homologous waves are 257 ± 22 km s^{-1} (wave 1), 219 ± 18 km s^{-1} (wave 2), 249 ± 18 km s^{-1} (wave 3), and 337 ± 31 km s^{-1} (wave 4). All peak perturbation profiles together with a Gaussian fit are shown in Figure 4 (top panel). The perturbation profiles of all four waves are steepening and show an increase in amplitude in the early phase of their evolution until the peak perturbation amplitude $A_{\max}$ is reached. The values $A_{\max}$ of all four waves are 1.15 (wave 1), 1.1 (wave 2), 1.14 (wave 3), and 1.24 (wave 4).

The bright fronts of coronal EUV waves are in general caused by a local temperature and density enhancement (plasma compression). Assuming that the change in density is more important than that in temperature, one can derive an estimate of the density jump from the intensity amplitude $A = I/I_0$, $N/N_0 \sim (I/I_0)^{1/2}$. This implies for the peak amplitudes of the four homologous waves a maximum density jump of $X_c = N/N_0 = 1.07$ (wave 1), 1.05 (wave 2), 1.07 (wave 3), and 1.11 (wave 4).

3.3. Associated CMEs and Flares

The analysis of EUVI, COR1, and COR2 images, covering both days of April 28 and 29, revealed no clear evidence of associated CMEs. However, LASCO C2 recorded four faint CMEs, each entering the C2 FoV about 45 minutes after the first

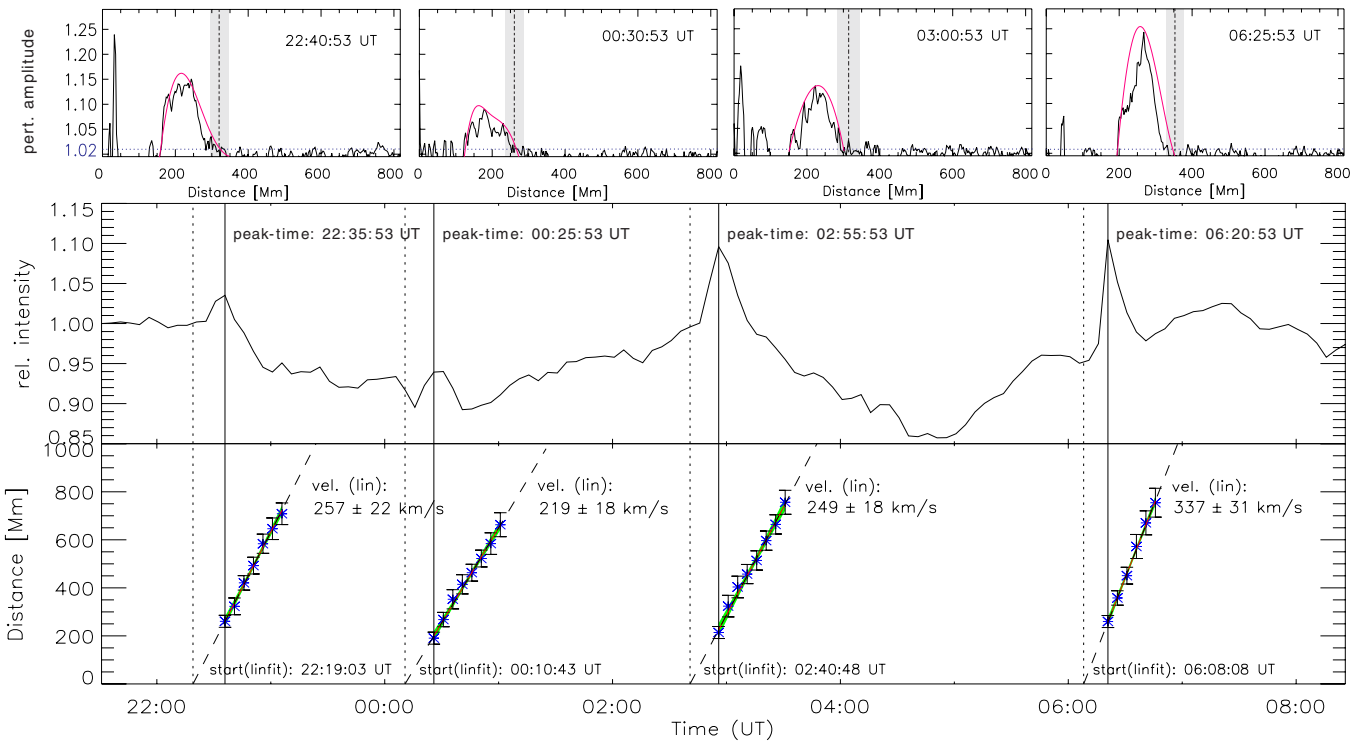

Figure 4. Top: 195 Å peak intensity enhancements ("perturbation profiles") of the four waves together with Gaussian fits derived from RR images in a 60° sector (cf. Figure 1; panel 7). Each vertical line indicates the distance of the visually tracked wave front, gray bars represent measured errors. Middle: variations of the flare intensity (in units of pre-event intensity; cf. Figure 2(g), yellow square). Bottom: time–distance diagram of all waves together with their linear fits. Green areas illustrate the 95% confidence bands for each linear fit. Note that the first wave fronts coincide with the flare peak intensity of the subfield.

observation of a wave front by EUVI (cf. Figures 2 (a)–(d) and animation 2B). In the LASCO CME catalog just CMEs 2–4 are listed and classified as poor, only visible in C2 at position angles ∼85°. CMEs 3 and 4 reveal additional bright features following the actual CME leading edge with at least the same speed. These features resemble rather small-scale ejecta than prominences trailing the leading edge and could be related to the above mentioned weak disturbances following waves 3 and 4 (see animation 1). As the center of the source AR lies ∼15° behind the limb, as seen from *SOHO*, we experience low projection effects in the derived CME plane-of-sky velocities, which lie in the range of 140–190 km s^{-1} (see Figure 2 (e)). Setting the onset site to the solar limb and onset time to the moment, EUVI observed the first front of the associated wave, we estimated for each of CMEs 2–4 an average initial velocity in the range of 370–470 km s^{-1}. We can speculate that the kinematics shown in Figure 2(e) supports the idea of a strong deceleration of the faint, i.e., low-density, CMEs during their early evolution.

In each of the four wave events, an increase in intensity in the central region of the source loop system (see Figure 2(g)), constituting weak flares, is observed ∼5 minutes before the first recorded wave front. Since the wave events occurred behind the solar limb, as viewed from Earth, no *GOES* X-ray data are available to obtain the flare class. As the determined wave kinematics allows us to back-extrapolate the start of the wave (see Figure 4, bottom panel), we can compare the timing of the flare commencement and the wave onsets (see also animation 2A). Figure 4 (middle panel) shows the evolution of the total intensity of the central region in the AR. Four distinct intensity peaks are discernible, which coincide with the first observations of the four coronal waves. During these flaring phases, we observe the disappearance of several loops in the 195Å RR-images (see Figure 2(f)), whose northern branch is rooted close to the flaring part of the AR. The coronal waves are, however, launched from the opposite side and the shape of each first wave front exactly maps out the geometry of the southern loop system.

4. DISCUSSION AND CONCLUSIONS

Never before in the nearly 14 years of continuous research of large-scale coronal waves were homologous EIT wave events reported. We are the first to present a study of homologous EIT waves, emerging from the same AR within a short period of time. They travel into the same direction and their fronts have similar shape and angular extent. They propagate into a quiet-Sun area, surrounded by ARs to the north and south and a large coronal hole close to the northern polar region (see animation 1). As is expected for nonlinear magnetosonic waves, they do not penetrate into these regions of increased Alfvén velocity (see also Veronig et al. 2008; Gopalswamy et al. 2009). In our study, we compared for the first time different methods of deriving the wave kinematics, the (rather subjective) visual method and the (more objective) profile method. Both methods yield consistent results, i.e., the waves propagate at constant velocities ∼220 km s^{-1} for the weakest wave up to ∼340 km s^{-1} for the strongest event. Furthermore, we calculated the perturbation profiles to study the physical characteristics and evolution of the disturbances. The strong initial steepening of the perturbation amplitudes confirms that these features are indeed shocks, albeit only weak shocks, since they peak at low-intensity values $A < 1.25$.

Assuming these coronal waves to be large-scale fast magnetosonic waves, the measured velocities lie well within the velocity range of 210–350 km s^{-1} for fast magnetosonic waves for quiet-Sun conditions. In the MHD approach, the quanti-

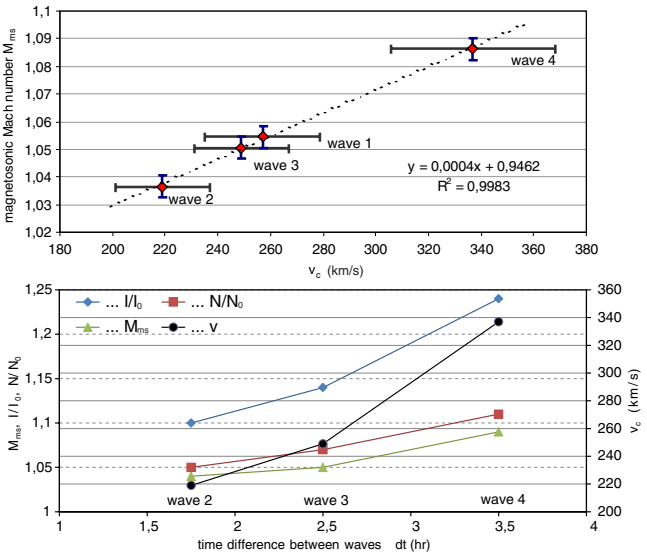

Figure 5. Top: correlation between magnetosonic Mach numbers $M_{\rm ms}$, derived from peak perturbation amplitudes, and linear propagation velocities $v_{\rm c}$ of the four coronal waves. Error bars in the Mach numbers are determined by the uncertainties in the Gaussian fits to the perturbation amplitudes (see Figure 4, top panels). Bottom: intensity amplitude (I/I_0), density amplitude (N/N_0), Mach number ($M_{\rm ms}$), and wave velocity ($v_{\rm c}$) presented as a function of the time lags between successive waves.

ties defining a shock wave in the solar corona are as follows: $M_{\rm ms}$, shock magnetosonic Mach number; $X_{\rm c}$, density jump at the shock front; ϑ, angle between shock front and magnetic field; $\beta_{\rm c}$, plasma-beta. They are related by the Rankine–Hugoniot (RH) conditions for an oblique shock (cf. Priest 1982). Considering a perpendicular shock the RH relation reduces to

$$M_{\rm ms} = \sqrt{\frac{X_{\rm c}(X_{\rm c}+5+5\beta_{\rm c})}{(4-X_{\rm c})(2+\gamma\beta_{\rm c})}},$$

with a polytropic index γ of 5/3. Studies of Vršnak et al. (2002) indicate that $\beta \approx 0.1$ in the quiet-Sun's low corona. Using the previously calculated density jumps X_c (cf. Section 3.2, $X_c \propto \sqrt{A}$), we derive for the peak magnetosonic Mach numbers $M_{\rm ms} = 1.06$ (wave 1), 1.04 (wave 2), 1.05 (wave 3), and 1.09 (wave 4).

With these observations of homologous waves, we can for the first time perform a quantitative analysis of the characteristic wave parameters without any limiting factors like changing or unknown quiet-Sun background conditions. The top panel of Figure 5 shows the calculated magnetosonic Mach number versus the propagation velocities $v_{\rm c}$ of the four waves, revealing a distinct correlation between the wave characteristics $M_{\rm ms}$ and $v_{\rm c}$ with a correlation coefficient of $R^2 \approx 0.99$. Such correlation is expected for nonlinear fast-mode magnetosonic waves because of the relation $M_{\rm ms} = v_{\rm c}/v_{\rm ms}$ (cf. Priest 1982), where $v_{\rm c}$ is the coronal wave speed and $v_{\rm ms} = \sqrt{v_{\rm A}^2+c_{\rm s}^2}$ the fast magnetosonic speed (where $v_{\rm A}$ is Alfvén velocity and $c_{\rm s}$ is sound speed). The mean magnetosonic speed, derived by averaging the four ratios $v_c/M_{\rm ms}$, yields 250 km s^{-1} and gives with $c_s = 180$ km s^{-1} ($T \sim 1.5$ MK) a mean Alfvén velocity of $v_{\rm A} = 175$ km s^{-1}. Applying one- to five-fold Saito coronal density models for a propagation height of $\sim 0.1\,R_\odot$, we derive for the low corona during solar minimum conditions a magnetic field strength between 1.5 and 3.5 G.

The magnetosonic Mach numbers of all four waves peak at values less than 1.10 and drop off toward the linear regime ($M_{\rm ms} \approx 1$) as the waves expand. These small magnetosonic Mach numbers together with the correlated wave velocities support the view that each observed coronal wave is a low-amplitude MHD fast-mode wave. Since $M_{\rm ms}$ is even at the maximum close to the linear regime, this also implies that the fast-mode MHD waves are expected to experience only minor deceleration. Since $v_{\rm c}$ decreases proportional to $M_{\rm ms}$, this implies a <10% change in velocity for the waves under study. For the strongest wave 4 this corresponds to a value of $\sim$30 km s^{-1}. As the error in velocity is of the same order of $\sim$10% ($\sim \pm 30$ km s^{-1} for wave 4), such weak deceleration is hidden in the measurement uncertainties. Finally, we note a clear correlation between the lags between successive waves, interpreted as the buildup times of the magnetic energy for the following wave event, and the intensity I/I_0, density N/N_0, magnetosonic Mach number $M_{\rm ms}$, and the propagation velocities $v_{\rm c}$ of waves 2–4 (cf. Figure 5, bottom).

In our study of the homologous wave events, it was possible to compare the wave pulse characteristics and analyze correlations between the wave parameters, knowing that the four large-scale waves propagate in similar coronal conditions. This means that any found correlation is independent from the indeterminate but constant coronal conditions. Our results provide strong support that the observed large-scale coronal waves are indeed fast-mode magnetosonic waves, and additionally suggest a dependence of the wave parameters upon the buildup time of the magnetic energy.

I.W.K., A.M.V., and N.M. acknowledge the Austrian Science Fund (FWF): P20867-N16. The European Community's Seventh Framework Programme (FP7/2007-2013) under grant agreement no. 218816 (SOTERIA) is acknowledged (B.V., M.T.). We thank the *STEREO*/SECCHI teams for their open data policy.

REFERENCES

Attrill, G. D. R., Harra, L. K., van Driel-Gesztelyi, L., & Démoulin, P. 2007, ApJ, 656, L101
Biesecker, D. A., Myers, D. C., Thompson, B. J., Hammer, D. M., & Vourlidas, A. 2002, ApJ, 569, 1009
Brueckner, G. E., et al. 1995, Sol. Phys., 162, 357
Chen, P. F., Wu, S. T., Shibata, K., & Fang, C. 2002, ApJ, 572, L99
Cohen, O., Attrill, G. D. R., Manchester, W. B., & Wills-Davey, M. J. 2009, ApJ, 705, 587
Delaboudinière, J.-P., et al. 1995, Sol. Phys., 162, 291
Delannée, C., & Aulanier, G. 1999, Sol. Phys., 190, 107
Gopalswamy, N., et al. 2009, ApJ, 691, L123
Howard, R. A., et al. 2008, Space Sci. Rev., 136, 67
Kaiser, M. L., Kucera, T. A., Davila, J. M., St. Cyr, O. C., Guhathakurta, M., & Christian, E. 2008, Space Sci. Rev., 136, 5
Kienreich, I. W., Temmer, M., & Veronig, A. M. 2009, ApJ, 703, L118
Klassen, A., Aurass, H., Mann, G., & Thompson, B. J. 2000, A&AS, 141, 357
Long, D. M., Gallagher, P. T., McAteer, R. T. J., & Bloomfield, D. S. 2008, ApJ, 680, L81
Moses, D., et al. 1997, Sol. Phys., 175, 571
Muhr, N., Vršnak, B., Temmer, M., Veronig, A. M., & Magdalenić, J. 2010, ApJ, 708, 1639
Patsourakos, S., & Vourlidas, A. 2009, ApJ, 700, L182
Podladchikova, O., & Berghmans, D. 2005, Sol. Phys., 228, 265
Priest, E. R. 1982, Solar Magneto-hydrodynamics (Dordrecht: Reidel), 74
Thompson, B. J., Plunkett, S. P., Gurman, J. B., Newmark, J. S., St. Cyr, O. C., & Michels, D. J. 1998, Geophys. Res. Lett., 25, 2465
Thompson, B. J., et al. 1999, ApJ, 517, L151
Veronig, A. M., Muhr, N., Kienreich, I. W., Temmer, M., & Vršnak, B. 2010, ApJ, 716, L57
Veronig, A. M., Temmer, M., & Vršnak, B. 2008, ApJ, 681, L113
Veronig, A. M., Temmer, M., Vršnak, B., & Thalmann, J. K. 2006, ApJ, 647, 1466

Vršnak, B., & Cliver, E. W. 2008, Sol. Phys., 253, 215
Vršnak, B., Warmuth, A., Brajša, R., & Hanslmeier, A. 2002, A&A, 394, 299
Wang, Y.-M. 2000, ApJ, 543, L89
Warmuth, A. 2010, Adv. Space Res., 45, 527
Warmuth, A., Vršnak, B., Magdalenić, J., Hanslmeier, A., & Otruba, W. 2004, A&A, 418, 1101
Wills-Davey, M. J. 2006, ApJ, 645, 757
Wills-Davey, M. J., & Attrill, G. D. R. 2009, Space Sci. Rev., 149, 325
Wills-Davey, M. J., & Thompson, B. J. 1999, Sol. Phys., 190, 467
Wu, S. T., Zheng, H., Wang, S., Thompson, B. J., Plunkett, S. P., Zhao, X. P., & Dryer, M. 2001, J. Geophys. Res., 106, 25089
Wuelser, J., et al. 2004, Proc. SPIE, 5171, 111